

In-phase sub-Nyquist lenslet arrays encoded onto spatial light modulators

IGNACIO MORENO,^{1,2,*} DON M. COTTRELL,³ JEFFREY A. DAVIS,³ MARÍA M. SÁNCHEZ-LÓPEZ,^{1,4} AND BENJAMIN K. GUTIERREZ³

¹*Instituto de Bioingeniería, Universidad Miguel Hernández de Elche, 03202 Elche, Spain*

²*Departamento de Ciencia de Materiales, Óptica y Tecnología Electrónica, Universidad Miguel Hernández de Elche, 03202 Elche, Spain*

³*Department of Physics, San Diego State University, San Diego, California 92182-1233, USA*

⁴*Departamento de Física Aplicada, Universidad Miguel Hernández de Elche, 03202 Elche, Spain*

*i.moreno@umh.es

Abstract: When encoding diffractive lenses onto a spatial light modulator (SLM), there is a Nyquist limit to the smallest focal length that can be formed. When this limit is surpassed, a two-dimensional array of lenslets is formed. There have been very few discussions of the performance of these lenslets. In this work, we focus on the phase distribution of these lenses in the array. We show that, for certain values of the focal length, the lenslets are all in perfect phase. We show that this situation happens for a total number of $N/4$ discrete equidistant sub-Nyquist different focal lengths, where $N \times N$ is the number of pixels in the SLM. We find other distances in between where the array is composed of two sets of lenslets with a relative π phase among them. Finally, we illustrate these phase distributions in the application to generate an array of vortex producing lenses. We expect that these results might be useful for high accuracy interferometric or multiple imaging where this phase must be exactly the same for each replica.

© 2020 Optical Society of America

1. Introduction

Modern liquid crystal spatial light modulators (SLM) [1] have resulted in 2D pixelated arrays with thousands of pixels and pixel dimensions about a few microns. This high resolution motivated their use in optical processing, pioneered in [2]. SLMs are nowadays used routinely to display dynamic diffractive optical elements (DOE) in all types of applications [3].

One of the easiest and most useful applications of SLMs is the capability to encode diffractive lenses. Lenses can be made as converging or diverging, and anamorphic lenses can also be easily encoded. However, there are limits to the smallest focal lengths that can be encoded because of the limited spatial resolution. These occur because the period of the quadratic phase function decreases as the focal length decreases.

Some time ago [4], our group defined this Nyquist limit for the shortest focal length that can be encoded on the SLM when this smallest period equals two pixels. In that work, we examined lenses where the focal length was much shorter than the Nyquist limit. We found that this process forms a lenslet array that produces several equally intense focal points. We were also able to encode the Fourier transform of an object onto the lenslet array. In this case, we showed that each of the lenses formed the Fourier transform producing an array of identical images. Although it was noticed that the phases on each lens were different and it was realized that there would be phase shifts in the encoded output points, these early works were centered on the intensity of the multiple focal spots using binary-phase SLM devices [4,5].

However, the great advances in micro-optics technology and in SLM technology, led to a renovated interest in micro-lens arrays (MLA) in applications such as wave-front sensors [6], integral imaging [7], multiple optical trapping [8], or miniature interferometers for nano-metrology [9]. In these applications, the intensity, but also the phase shift of the focus spots can

be relevant in their correct performance. This might also be of interest in holographic imaging approaches because the interference between the reference beam and each beam from the array would change [10], or in detector arrays with improved fill factor where diffractive microlenses are employed to increase the concentration factor [11].

In this work, we analyze the phase-shift between these multiple lenses in the lenslet array that is generated with a sub-Nyquist encoded lens, in this case using a continuous phase-only SLM. Analytical expressions are derived for the phase-shift at each sublens, and the conditions for all of them to be in-phase are found. For a SLM containing $N \times N$ pixels, we find that there is a total number as large as $N/4$ of different sub-Nyquist focal lengths that fulfill this condition. We show how to control the relative phases of the lenses.

Another area where these lenslet arrays are of interest is in the field of vortex and vector beams. Recently there has been reports of the fabrication of micro-arrays for the parallel processing of orbital angular momentum [12]. It is well known that the combination of a lens function and a spiral phase function produces a spiral lens pattern generating vortex beams [13]. Vortex microlens arrays have been fabricated using combined refractive/diffractive techniques [14]. However, we show here that sub-Nyquist vortex lenses only generate the vortex beam in the central lens. Thus, we propose a simple alternative technique to effectively generate vortex beams in all of the sub-lenses in the array. We show that the same conditions for relative phase-shifts between sub-lenses hold in this situation compared to the standard one, and all in-phase vortex beam arrays are generated with the same values of the encoded focal lengths.

In all cases we show experimental evidence of the phase-shift between sub-Nyquist lenslet arrays. For that purpose, we use a simple common-path polarization interferometer based on the liquid-crystal SLM itself [15].

The paper is organized as follows: after this introduction section, we include a theoretical section that reviews the mathematics of lenses with the sub-Nyquist focal lengths and the phase relationships between the various sub-lenses in the generated array. Next, we review our experimental system and its configuration as a common-path polarization interferometer. We show experimental results where we vary the phase relationships between the various focal spots. Next, in Section 4, we show how to add a spiral phase to each of the lenslets in order to generate an array of vortex beams. Finally, we present the conclusions of the work.

2. Theory for sub-Nyquist focal length lenses encoded onto SLMs

A converging Fresnel lens is generated onto a phase-only SLM by writing a quadratic phase-only function $Z^*(f)$ that depends of the desired focal length (f) and the wavelength (λ) of the inut light as

$$Z^* = \exp\left\{\frac{i\rho(x^2 + y^2)}{f}\right\} = \exp\left\{\frac{i\rho D^2(p^2 + q^2)}{f}\right\}. \quad (1)$$

Here (x, y) denote the spatial coordinates on the SLM, typically measured in microns. We rewrite these positions in terms of the SLM pixel spacing D as $x = pD$ and $y = qD$, where (p, q) are integer numbers, $p, q = -(N/2) + 1, \dots, -1, 0, +1, \dots, N/2$, where $N \times N$ denotes the number of pixels in the SLM array.

As stated earlier, the phase steps become closer as we move to the edge of the array. Accordingly, we defined [4] the Nyquist limit focal length f_N as the focal length that gives a a period of two pixels at the edge of the SLM, leading to

$$f_N = \frac{ND^2}{f}. \quad (2)$$

Figure 1(a) shows the lens phase function at this limiting focal length, represented in an array with $N = 1024$, assuming a wavelength of $\lambda = 0.6328$ microns and a pixel spacing of $D = 20$ microns, that reproduce our experimental conditions. In this case the Nyquist focal length is $f_N = 647.282$ mm. Note how the aliasing starts to give secondary lenses at the edges and at the corners of the image.

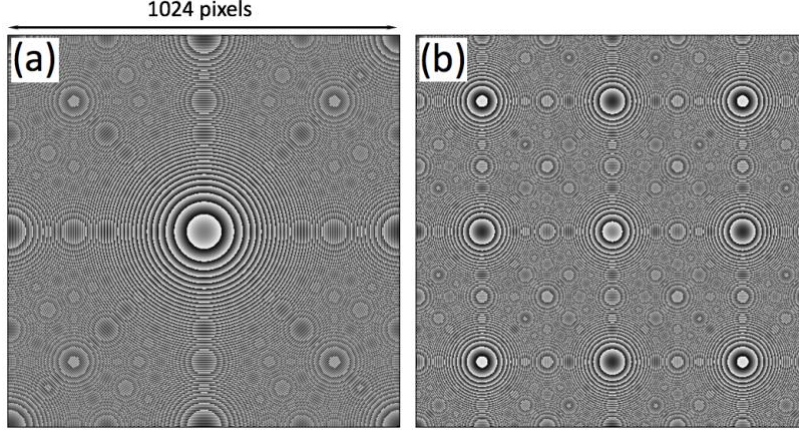


Fig. 1. Phase patterns for a lens (a) having the Nyquist focal length f_N and (b) having a focal length of $f = f_N / 3$. The lens is encoded with $N = 1024$.

Now we consider the case where the focal lengths are smaller than this as $f = af_N$. An example is shown in Fig. 1(b) where $a = 1/3$. We see an array of 3×3 lenses. However, we note in Fig. 1(b) that there are phase differences between these lenses. These differences are shown by the fact that the central area of each lens has a different gray level corresponding to a different phase shift. This will not affect the intensity of the focused spots, but introduce problems if we wanted to form focused spots or images with identical relative phase.

We can examine these conditions more closely. Examining Eq. (1), we see that it can be rewritten as:

$$Z^* = \exp\left\{\frac{i\rho D^2(p^2 + q^2)}{lf}\right\} \exp\{-i2\rho(pm + qn)\}, \quad (3)$$

where (m, n) are integer values so the second exponential term in Eq. (3) is simply multiplying the lens pattern by one. Equation (3) can be further developed to read as

$$\begin{aligned} Z^* &= \exp\left\{\frac{i\rho D^2}{lf}\left[p^2 + q^2 - 2(pm + qn)\frac{lf}{D^2}\right]\right\} = \\ &= \exp\left\{\frac{i\rho D^2}{lf}\left[\left(p - m\frac{lf}{D^2}\right)^2 + \left(q - n\frac{lf}{D^2}\right)^2\right]\right\} \exp\left\{-\frac{i\rho lf}{D^2}(m^2 + n^2)\right\}. \end{aligned} \quad (4)$$

Therefore, this shows that replications of the central Fresnel zone function will occur at coordinates that satisfy

$$(x_m, y_n) = \left(m\frac{lf}{D}, n\frac{lf}{D}\right) = (maND, naND), \quad (5)$$

where we used the relations that $f = af_N = aND^2/l$. This indicates that these replicas will be separated in the (x, y) plane by distances of

$$\frac{lf}{D} = aND. \quad (6)$$

In addition, Eq. (4) shows that these replica zone functions will have relative phases given by

$$f_{mn} = -\frac{\rho lf}{D^2}(m^2 + n^2). \quad (7)$$

Therefore, note that all of these zone functions will be in phase provided that

$$\frac{\rho lf}{D^2} = \frac{\rho laf_N}{D^2} = 2\rho k. \quad (8)$$

Here k is an integer. Using the definition of the Nyquist focal length in Eq. (2), this sets requirements on the focal lengths that are satisfied by a discrete number of distances f_k , given by

$$f_k = \frac{2D^2}{l}, \frac{4D^2}{l}, \frac{6D^2}{l} \dots \frac{ND^2}{l}. \quad (9)$$

which, written in terms of the Nyquist focal length, are given by

$$f_k = \frac{2k}{N}f_N. \quad (10)$$

where now $a = 2k/N$. Thus, note that there are $N/4$ different focal length distances that satisfy these conditions, all equally separated by a distance

$$df = \frac{2D^2}{l}. \quad (11)$$

We also note that there is another set of distances in between for which the lenses in the array will be out of phase when the focal length is displaced by $df/2$ from the values in Eq. (9).

We examine these conditions. We again assume a wavelength of $l = 0.6328$ microns, a pixel spacing of $D = 20$ microns, and an SLM with 1024×1024 pixel array, i.e. with a Nyquist focal length of $f_N = 647.282$ mm. Next, we show two examples. Figure 2(a) shows only the central area of 256×256 pixels of the phase pattern created for a focal length of $f = f_N/16 = 40.455$ mm corresponding to $f = 54D^2/l$ from Eq. (9) or $k = 32$ in Eq. (10). Note how all the lenses in the array in phase.

By contrast, Fig. 2(b) shows the case where the adjacent lenses are out of phase and corresponding to a focal length of $f = (f_N/16) + (df/2) = 41.087$ mm. This focal length is displaced by $df/2 = D^2/l = 0.632$ mm, according to Eq. (11). Similar results were found for the shorter focal length of $f = (f_N/16) - (df/2) = 39.823$ mm. Therefore, for these distances, the complete lenslet array can be regarded as composed by two complementary arrays with lenses aligned diagonally, separated by distances $\sqrt{2}l/D$ and with a relative π phase shift between them.

At intermediate focal lengths, the relative phase shifts change between these two situations.

Before discussing other results, we will discuss our experimental setup. That will allow us to examine the agreement between theory and experiment in a more convenient way.

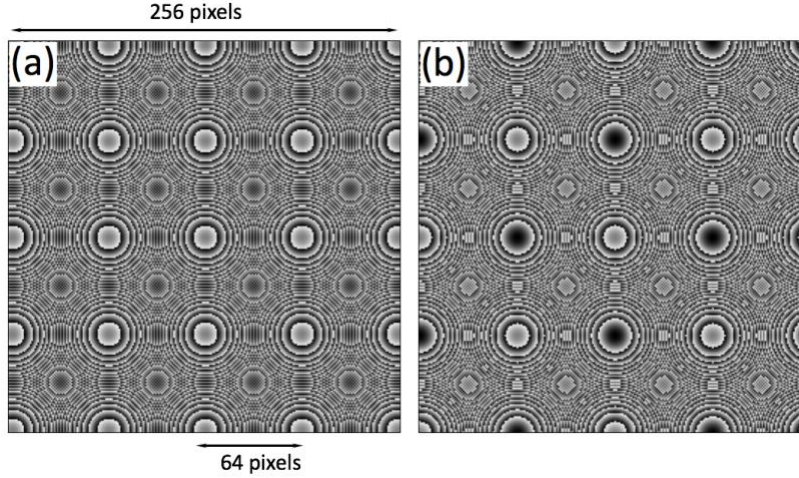


Fig. 2. Phase patterns for (a) a lens having the focal length of $f = f_N / 16 = 40.455$ mm and (b) a lens having a focal length of $f = f_N / 16 + df / 2 = 41.087$ mm. Only the central 256×256 pixels are shown.

3. Experimental setup

In our experimental setup shown in Fig. 3, light from a He-Ne laser is spatially filtered and collimated and is sent through a 2" non-polarizing beamsplitter (NPBS) to a reflective liquid-crystal on silicon (LCoS) SLM device. We used a Hamamatsu LCoS device (model X10468-01) designed for the visible range and having a phase modulation depth of more than 2π at the He-Ne laser wavelength of $\lambda = 0.6328$ microns. These devices are characterized by displays of 792×600 pixels with a pixel spacing of $\Delta = 20$ μm . The light is reflected by the LCoS-SLM device, and passes again through the NPBS to a WinCam detector. The input beam has a circular shape with a diameter of about 7.5 mm, corresponding to less than 400 pixels. Within this area we did not observe a significant aberration effect from the beam splitter or from the LCoS-SLM backplane.

The lens patterns are generated on a 1024×1024 pixel array. The output from the computer goes to an electronic splitter and then to both the LCoS-SLM and a monitor. We overfill the display in both directions. In most cases, the short focal lengths form images within the NPBS. So, we used a 20 cm focal length lens (L2) to image these patterns onto the detector with the additional advantage that the output fit within the sensitive area of the detector.

We employed a self-referencing interferometer technique [15] for examining the relative phase shifts for each focus. We introduced a polarizer (P1) in the incident beam so that there was a vertical component oriented perpendicular to the director axis. This component is not affected by the LCoS-SLM and is the reference beam in the interferometer, while the horizontally oriented component would have the lenslet array encoded onto it. Then we place another polarizer (P2) in front of the detector that allowed parallel components of these two beams to interfere. We deliberately put the images slightly out of focus in order to decrease their intensity and to make the interference more visible.

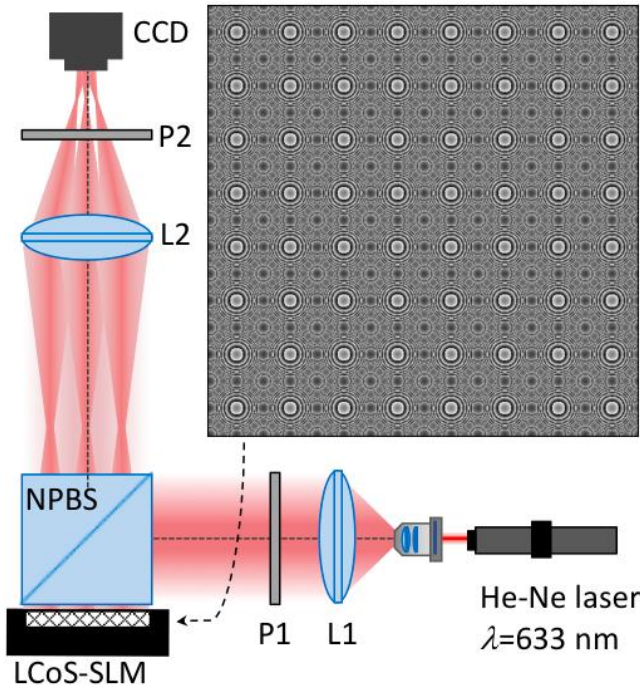


Fig. 3. Scheme of the optical setup.

4. Experimental results

Figure 4(a) shows the experimental capture at the CCD detector corresponding to the output for the array shown in Fig. 2(a) with the focal length of 40.455 mm. The experiment shows a background corresponding to the reference beam (polarization component perpendicular to the liquid-crystal director), and shows the interference with the spherical waves originated at the lenses in the array. It is clear that all of the focus points have the same phase.

By contrast Fig. 4(b) shows the output for the array in Fig. 2(b) using a focal length of 41.087 mm (i.e., when the focal length is displaced by $df/2$). Again, it is obvious that adjacent focus spots have π phase shifts. We note that a similar pattern to Fig. 4(b) was also seen for a focal length of 39.823 mm. Note that the number of lenslets in the array is the same since there is only a very small variation of less than 0.02 microns in the distance between lenslets in the two cases shown in Fig. 4.

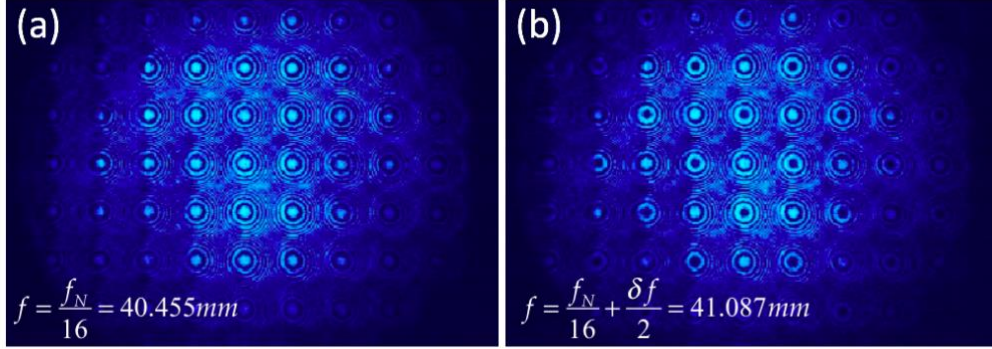


Fig. 4. Experimental output interference patterns for (a) lens array from Fig. 2(a) at a focal length of 40.455 mm, with all lenslets in phase (b) lens array from Fig. 2(b) at a focal length of 41.087 mm, with two subsets of lenslets out of phase.

We can also examine intermediate distances. Figures 5(a) and 5(b) show the interference patterns at intermediate focal length distances of 40.139 mm and 40.771 mm. These arrays are obtained by shifting the focal length by a quarter of δf on either side of the pattern in Fig. 4(a) with focal length of 40.455 mm. This involves shifting the focal length by a total of only 0.316 mm. Although the result looks similar to that in Fig. 4, there are several subtle differences that we discuss where we emphasize the central 3×3 spots.

First, we see that now the diagonal spots are out of phase with respect to the central spot. In addition, the four spots that are above, below, left, and right of the central spot shift their phase relationship from $+\pi/2$ to $-\pi/2$. These variations are caused by the different phase values at each sublens (m, n) given by the term $(m^2 + n^2)$ in Eq. (7).

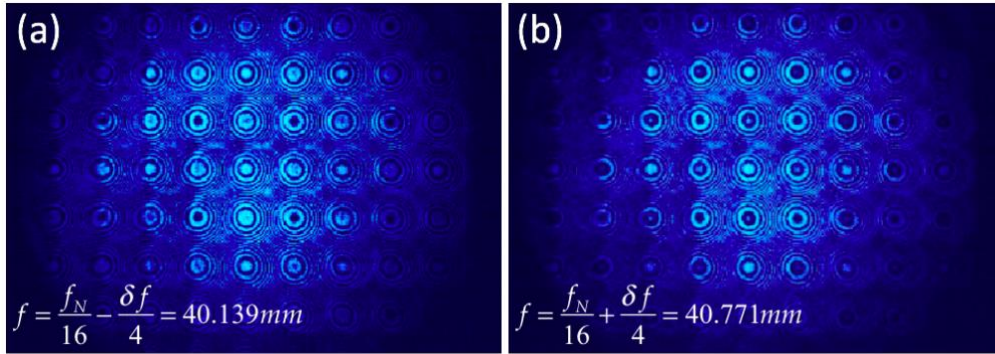


Fig. 5. Output interference patterns for (a) lens array at a focal length of 40.139 mm, (b) lens array at a focal length of 40.771 mm.

5. Encoding vortices onto each focus

Next, we wanted to encode a lenslet array where each focus creates a vortex beam. We again used the focal length of $f = f_N / 16 = 40.455$ mm shown in Fig 2(a). We found that, if we simply multiplied the lens by a spiral phase, only the central lens shows the characteristic spiral pattern of a diffractive vortex lens [13] as shown in Fig. 6(a). The rest of the lenses created by the sub-Nyquist array effect do not show the spiral pattern and they all appear as regular lenses, but with a relative phase factor among them that changes azimuthally. This figure shows only the central 256×256 pixels area in order to more clearly see the differences. Therefore, a

vortex beam would be created only in the central focalization, which will have a typical doughnut shape, while the rest of the focal points will have the usual bright spot.

However, we used a trick to overcome this limitation and generate an array of vortex lenses. The sequence was as follows. We created the lens, took its Fourier transform, multiplied this by a spiral phase in the Fourier domain, took the inverse Fourier transform, and finally divided by the magnitude to create the phase-only pattern that can be displayed on the SLM. The result in Fig. 6(b) shows that this was successful and now all the lenses in the array exhibit the spiral pattern, thus all of them creating a vortex beam. This process can be explained as now producing the convolution of the original lenslet array with the spiral phase pattern, thus replicating the spiral pattern on each sublens of the array. Also note that, since we started from a lenslet array where all the lenses were in phase, this situation persists in the vortex array. This is visible in the fact that every spiral lens has the starting point of the spiral in the same angle.

Next, we examined the results when we changed the focal length to $f = (f_N / 16) - (df / 2) = 39.823\text{mm}$, where the adjacent lenses have a relative π phase-shift. Figure 6(c) shows this case and it shows clearly how adjacent lenslets are out of phase. Since the spiral phase mask is an azimuthal grating, the π phase shift has the effect of rotating the origin of the spiral phase mask by 180° . Figure 6(c) shows that adjacent spiral phase masks have this rotational difference.

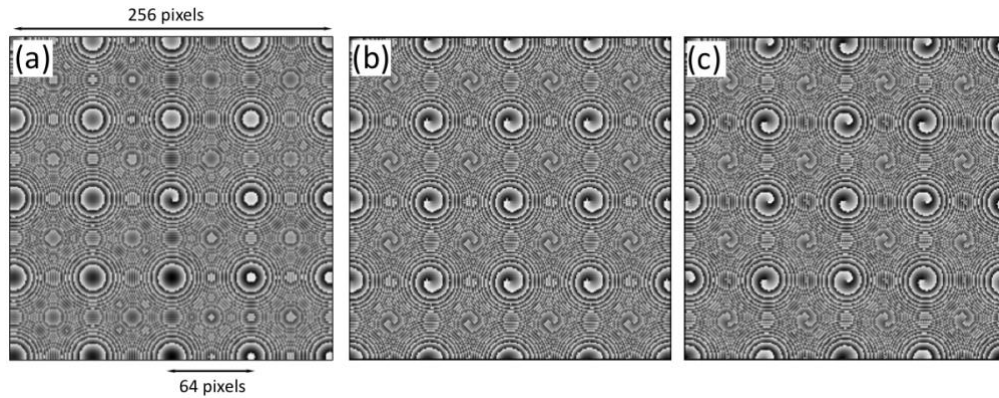


Fig. 6. Phase masks comparing the case where (a) the lenslet array is multiplied by the spiral phase function and (b) the convolution of the two functions. In both cases, we used a focal length of 40.455 mm to have an array in phase. (c) Showing the same case as in (b) but now with the focal length of 39.823 mm to have an array out of phase. Only the central 256×256 pixels are shown.

Finally, we examine the experimental results for these arrays showing the interference between the reference beam and these vortex beams. Figure 7 shows the experiments corresponding to the patterns in Figs. 6(b) and 6(c). Experiments show that this approach is successful. In both cases the interferogram array shows spiral fringes verifying the effective generation of an array of vortex beams. In Fig. 7(a), the vortex beams in the array are all in phase, as it can be noticed because they all have the spiral interference pattern starting at the same angular position. On the contrary, the result in Fig. 7(b) exhibit the rotational difference of 180 degrees in the spiral pattern in adjacent lenses, as expected.

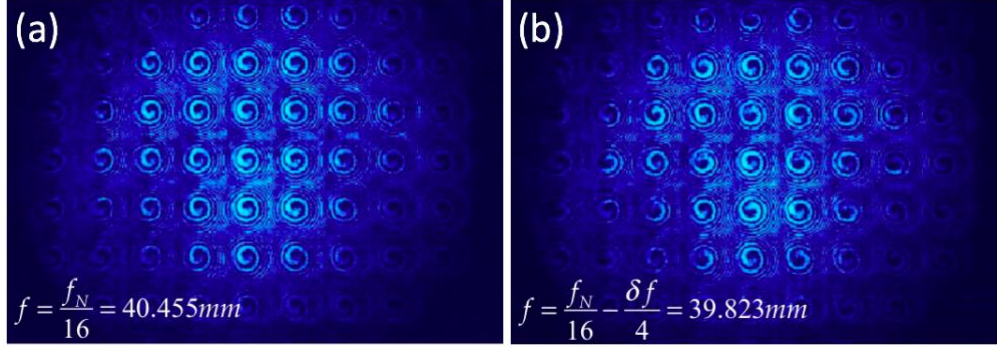


Fig. 7. Experimental interference patterns for the masks from Fig. 7(b) and 7(c). Images are captured in a defocused plane in order to visualize the interference pattern.

In Fig. 8 we provide additional results, captured at the plane where the beams focus. Here we present results of the central 3x3 spots, all three for the case with focal length $f = f_N / 16 = 40.455$. In Fig 8(a) no vortex is added, so the phase mask is that presented in Fig. 2(a). Now the standard bright focalization is observed in all spots. When we add the spiral phase and generate a phase mask like in Fig. 6(a), the central spot becomes the typical doughnut focus as shown in Fig. 8(b), but the rest remain as bright spots. In order to better visualize the effect, we added a spiral phase with topological charge $\ell = 6$ to create a circle with bigger diameter. Finally, in Fig. 8(c) we present the result when we follow the convolution process. Again a topological charge of $\ell = 6$ is applied. Note how now all spots successfully show the doughnut shape.

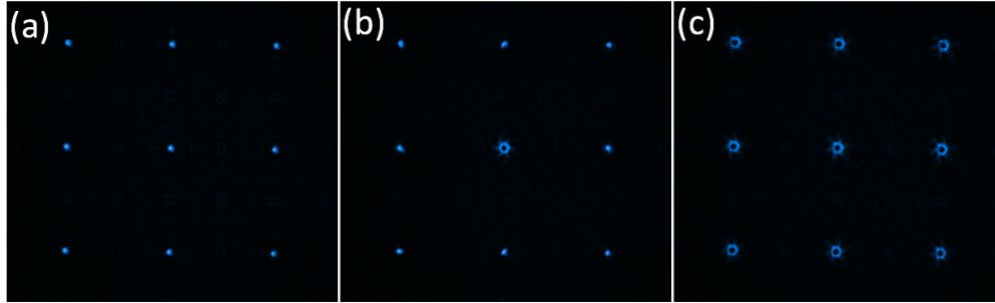


Fig. 8. Experimental focused plane for (a) a lens with focal length of 40.455 mm showing; (b) the same lens with an added spiral phase of topological charge $\ell = 6$; (c) equivalent result when the convolution procedure is applied. Only the central 3x3 focal spots are shown.

6. Conclusions

Past work on lenslet arrays generated by encoding sub-Nyquist lenses in SLMs was focused primarily on the intensity relation between the focal points. Although variations in the phase were noted, no further research was carried out in that direction. In this work, we investigated the phase distribution of these lenslets which lead to analytical expressions that can be used to produce arrays in which all lenslets and corresponding focal points are in perfect phase. We found that there are $N/4$ different sub-Nyquist focal distances that fulfill this condition, and they are equidistant. In addition, the focal distance intermediate between two consecutive such in-phase lenslet patterns generate a similar array but with two subsets of lenses out of phase.

Then we examined sub-Nyquist vortex lenses by adding a spiral phase to the lens pattern. We found that the lenslet array is generated as well, but only the central lens exhibits the spiral

pattern. Instead, we achieved a lenslet array which can produce vortex beams at all its foci by using a convolution procedure. This procedure demonstrated the successful realization of an array of vortex lenses. We then employed the equations previously derived to manipulate the phase distribution of adjacent vortex beams. This technique manifested itself as a 180° rotation in the spiral phase mask of adjacent lenslets. In all cases, results were confirmed experimentally.

Although this method of creating the lens array offers less flexibility than writing them independently, it offers a practical advantage of being faster and easier since it is not necessary to locate the points where each array would be located.

The results presented here have been validated with monochromatic light. When applications require the use of polychromatic light, other effects like chromatic aberration or wavelength dependent diffraction efficiency must be also considered. LCoS-SLMs with very large phase modulation, with various cycles of 2π phase modulation can be used to reduce the chromatic aberration [16].

These results suggest this technique can be applied to a variety of lenslet array DOE's. Applications where microlens arrays are employed can benefit from their physical realization with SLMs. These include, among others, wave-front sensing, integral imaging, optical trapping, nano-metrology or holographic imaging.

Funding

Ignacio Moreno and María M. Sánchez-López acknowledge funding from Conselleria d'Educació, Investigació, Cultura i Esport; Generalitat Valenciana (PROMETEO-2017-154); and Ministerio de Ciencia, Innovación y Universidades (Ministerio de Ciencia e Innovación (MICINN) (RTI2018-097107-B-C33).

Disclosures

The authors declare no conflicts of interest.

References

1. D. K. Yang and S.-T. Wu, *Fundamentals of Liquid Crystal Devices*, 2nd Edt., New York, Wiley (2015).
2. H. K. Liu, J. A. Davis, and R. A. Lilly, "Optical-data-processing properties of a liquid-crystal television spatial light modulator," *Opt. Lett.* **10**(12), 635–637 (1985).
3. T. Haist and W. Osten, "Holography using pixelated spatial light modulators—part 1: theory and basic considerations," *J. Micro/Nanolithogr MEMS MOEMS* **14**(4), 041310 (2015).
4. D. M. Cottrell, J. A. Davis, T. R. Hedman, and R. A. Lilly, "Multiple imaging phase-encoded optical elements written as programmable spatial light modulators," *Appl. Opt.* **29**, 2505 (1990).
5. E. Carcolé, J. Campos and S. Bosch, "Diffraction theory of Fresnel lenses encoded in low-resolution devices," *Appl. Opt.* **33**(2), 162-174 (1994).
6. M.-K. Park, H. Park, K.-I. Joo, T.-H. Lee, K.-C. Kwon, M.-U. Erdenebat, Y.-T. Lim, N. Kim, and H.-R. Kim, "Fast-switching laterally virtual-moving microlens array for enhancing spatial resolution in light-field imaging system without degradation of angular sampling resolution," *Sci. Reports* **9**, 11297 (2019).
7. A. O. Yontem and L. Onural, "Integral imaging using phase-only LCoS spatial light modulators as Fresnel lenslet arrays," *J. Opt. Soc. Am. A* **28**(11) 2359-2375(2011).
8. D. Schäffner, T. Preuschoff, S. Ristok, L. Broziom, M. Schlosser, H. Giessen and G. Birkel, "Arrays of individually controllable optical tweezers based on 3D-printed microlens arrays," *Opt. Express* **28**(6), 8640-8645 (2020).
9. W.-S. Wang, M. Wiemer, J. Froemela, T. Enderlein, T. Gessner, J. Lullin, S. Bargiel, N. Passilly, J. Albero, and C. Gorecki, "Vertical integration of array-type miniature interferometers at wafer level by using multi-stack anodic bonding," *Proc. SPIE* **9890**, 989011 (2016).
10. N. T. Shaked, B. Katz, and J. Rosen, "Review of three-dimensional holographic imaging by multiple-viewpoint-projection based methods", *Appl. Opt.* **48**(34), H120-H136 (2009).
11. P. W. R. Connolly, X. Ren, A. McCarthy, H. Mai, F. Villa, A. J. Waddie, M. R. Taghizadeh, A. Tosi, F. Zappa, R. K. Henderson, and G. S. Buller, "High concentration factor diffractive microlenses integrated with CMOS single-photon avalanche diode detector arrays for fill-factor improvement", *Appl. Opt.* **59**(14), 4488-4498 (2020).
12. C. Loussert, K. Kushnir, and E. Brasselet, "Q-plates micro-arrays for parallel processing of the photon orbital angular momentum," *Appl. Phys. Lett.* **105**, 121108 (2014).

13. K. Crabtree, J. A. Davis, and I. Moreno, "Optical processing with vortex-producing lenses," *Appl. Opt.* **43**(6), 1360-1368 (2004).
14. Z.-N. Tian, X.-W. Cao, W.-G. Yao, P.-X. Li, Y.-H. Yu, G. Li, Q.-D. Chen, and H.-B. Sun, "Hybrid refractive-diffractive optical vortex microlens," *IEEE Photonics Technol. Lett.* **28**(21), 2299-2302 (2016).
15. J. B. Bentley, J. A. Davis, J. Albero, and I. Moreno, "Self-interferometric technique for visualization of phase patterns encoded onto a liquid-crystal display," *Appl. Opt.* **45**(30), 7791-7794 (2006).
16. V. Calero, P. García-Martínez, J. Albero, M. M. Sánchez-López, I. Moreno, "Liquid crystal spatial light modulator with very large phase modulation operating in high harmonic orders", *Opt. Lett.* **38**(22), 4663-4667 (2013).